Site-independent strong phonon-vacancy scattering in high-temperature ceramics ZrB_2 and HfB_2

Vrishali Sonar,[1,2,*] Rohan Dehankar,[1,*] K. P. Vijayalakshmi,[3] Natalio Mingo,[4] and Ankita Katre[1,†]

[1]*Department of Scientific Computing, Modeling and Simulation, SP Pune University, Pune 411007, India*
[2]*Department of Physics, Adam Mickiewicz University, 61-614 Poznàn, Poland*
[3]*Vikram Sarabhai Space Centre, Kochuveli, Thiruvananthapuram 695022, India*
[4]*Université Grenoble Alpes, CEA, LITEN, 17 rue des Martyrs, 38054 Grenoble Cedex 9, France*

(Received 11 March 2022; revised 24 May 2022; accepted 27 May 2022; published 10 June 2022)

Similar effects of metal and boron vacancies on phonon scattering and lattice thermal conductivity (κ_l) of ZrB_2 and HfB_2 are reported. These defects challenge the conventional understanding that associates larger impacts to bigger defects. We find the underlying reason to be a strong local perturbation caused by boron vacancy that substantially changes the interatomic force constants. In contrast, a long ranged but weaker perturbation is seen in the case of metal vacancy. We show that these behaviors originate from a mixed metallic and covalent bonding nature in the metal diborides. The thermal transport calculations are performed in a complete *ab initio* framework based on Boltzmann transport equation and density functional theory. Phonon-vacancy scattering is calculated using *ab initio* Green's function approach. Effects of natural isotopes and grain boundaries on κ_l are also systematically investigated, however we find an influential role of vacancies to explain large variations seen in the experiments. We further report a two-order of magnitude difference between the amorphous and pure-crystal limits. Our results outline significant material design aspects for these multifunctional high-temperature ceramics.

DOI: 10.1103/PhysRevMaterials.6.065403

I. INTRODUCTION

Transition metal diborides exhibit a unique range of properties. They have excellent mechanical features such as ultra high melting temperature (>2500 °C), high flexural strength of the order of few hundreds of MPa, hardness of few tens of GPa, and appreciable oxidation resistance [1–5]. Furthermore, they show good electrical and thermal transport [6,7]. Recently, they were investigated for superconductivity as well as thin film applications [8–13]. Thus, metal diborides are interesting for low- to ultrahigh-temperature applications [1,14,15].

ZrB_2 and HfB_2 have gained much attention recently due to their higher stability [1]. They are actively investigated for applications with a prime focus on thermal transport such as in aerospace vehicles, hypersonic flights, and thermal protective coating [16–19], demanding a good understanding of thermal transport in these materials.

Several experimental studies on the thermal conductivity of ZrB_2 and HfB_2 (collectively referred as MB_2 hereafter) are found in the literature [7,20,21]. Zhang *et al.* [7] measured diffusivity by photothermal radiometry technique and from that determined the total thermal conductivity (κ)—the sum of electronic (κ_e) and lattice thermal conductivity (κ_l). However, they found κ_e to be the significant contribution to κ, whereas κ_l is estimated $\sim$10 $Wm^{-1}K^{-1}$ at 300 K for both MB_2. A similar trend is found in other experiments too, while not much is mentioned about the purity of MB_2 samples except the grain sizes that are reported in μm range [21–23]. Inquisitively, a few experiments have shown deviation from this trend by reporting more than twice the κ_l values at room temperature [20]. From the computational perspective, Lawson *et al.* [6] implemented molecular dynamics approach. They reported a higher κ_l of 54 $Wm^{-1}K^{-1}$ for ZrB_2 and 70 $Wm^{-1}K^{-1}$ for HfB_2. For ZrB_2, *ab initio* study by Xiang *et al.* [24] reported even higher κ_l of 90 $Wm^{-1}K^{-1}$ at 300 K, whereas Yang *et al.* [25] found *ab initio* calculated κ_l to be 79 $Wm^{-1}K^{-1}$ and 49 $Wm^{-1}K^{-1}$ without and with phonon-electron scattering respectively. Thus, a large variability in κ_l results is seen in literature, where the calculations are consistently found higher than the experiments. One reason for this difference could be the presence of native defects that may appear unintentionally during sample synthesis. Recently, studies exploring the stability of metal and boron vacancy defects in transition metal diborides have also been reported [8,26,27], which raises the curiosity to understand their effects on κ_l of ZrB_2 and HfB_2.

In this paper, we present a detailed *ab initio* study of the lattice thermal transport in ZrB_2 and HfB_2. The crucial roles of vacancies on phonon scattering is investigated along with an understanding of the intrinsic phonon scattering as well as the effect of natural isotopes and grain boundaries. Scattering from the vacancies are calculated with *ab initio* Green's function approach based on **T**-matrix scattering theory. We find that the metal vacancies ($\square_M$) and boron vacancies ($\square_B$) show surprisingly similar phonon scattering strengths in both ZrB_2 and HfB_2, thus demonstrating a distinctive characteristic of "*vacancy site independence*" of the thermal transport in these

*These authors contributed equally to this work.
†ankitamkatre@gmail.com

materials. This behavior is further investigated by examining the vacancy created perturbations and we find a pronounced effect of the smaller $\square_B$ than the bigger $\square_M$ in both MB_2. Our results provide a tangible explanation for the κ_l variations seen in literature for ZrB_2 and HfB_2 [20,28]. Finally, amorphous limit results are discussed that give an estimate of the κ_l lower bound.

II. COMPUTATIONAL METHODOLOGY

Ab initio thermal transport calculations are performed using almaBTE code [29], with extended implementation of Green's function approach for defects as in Refs. [30–32]. The lattice thermal conductivity tensor $\boldsymbol{\kappa_l}$ at a given temperature T is calculated as [29,33,34]

$$\boldsymbol{\kappa_l} = \frac{1}{k_B T^2 N \Omega} \sum_{\lambda} n_{0_\lambda}(n_{0_\lambda}+1)(\hbar\omega_\lambda)^2 v_\lambda \otimes v_\lambda \tau_\lambda \qquad (1)$$

where ω is the phonon frequency, v the group velocity, n_0 the equilibrium occupation and τ the relaxation time for phonon mode λ. The normalisation factor includes unit-cell volume Ω and q-point mesh density N. Final κ_l is calculated here as an average of in-plane and cross-plane components of thermal conductivity tensor as $\kappa_l = \mathrm{tr}(\boldsymbol{\kappa_l})/3$. Total τ is given as

$$\tau_\lambda^{-1} = \sum_{\substack{m=\text{anh,}\\ \text{iso, def, ...}}} \tau_{\lambda,m}^{-1}$$

where the summation is over different phonon scattering mechanisms (m) for each phonon mode λ. For perfect infinite lattices of MB_2, we include only intrinsic three phonon scattering τ_{anh}^{-1} as described in Ref. [33]. Scattering through isotopic mass disorder τ_{iso}^{-1} is further included using the methodology by Tamura *et al.* in Refs. [35,36]. τ_{anh}^{-1} requires *ab initio* calculated third-order interatomic force constants (IFCs) for the crystal, whereas only second-order IFCs and natural abundances of stable isotopes are needed for τ_{iso}^{-1}.

Phonon scattering rates due to crystallographic point defects τ_{def}^{-1} are calculated using the expression obtained from **T**-matrix scattering theory and the Optical theorem as [30,37],

$$\tau_{\lambda,\text{def}}^{-1} = -f_{\text{def}} \frac{\Omega}{\Omega_{\text{def}}} \frac{1}{\omega_\lambda} \Im\{\langle\lambda \,|\, \mathbf{T} \,|\, \lambda\rangle\}. \qquad (2)$$

where f_{def} is the number fraction of defects and Ω_{def} the volume of a defect. The **T** matrix is given as

$$\mathbf{T} = (\mathbf{I} - \mathbf{V}\mathbf{g}^+)^{-1}\mathbf{V} \qquad (3)$$

where $\mathbf{g}^+$ is the Green's function for perfect crystal, **I** the identity matrix, and **V** the perturbation matrix illustrating the differences between defect and perfect structures. **V** is the sum of IFC and mass perturbations, $\mathbf{V} = \mathbf{V}_K + \mathbf{V}_M$, where $\mathbf{V}_M$ is specially the on-site perturbation. In the case of vacancies, this on-site contribution is not relevant due to absence of atom at the defect site. Thus, we have $\mathbf{V} = \mathbf{V}_K$ only for $\square_M$ and $\square_B$ in MB_2. IFC perturbations are considered only up to third-nearest neighbor of every atom in a sphere of radius ~5 Å (6 NN) centered at the vacancy site. $\mathbf{V}_K$ is further corrected using an iterative scheme to annihilate the nonzero terms beyond the cut-off, as discussed in Ref. [30].

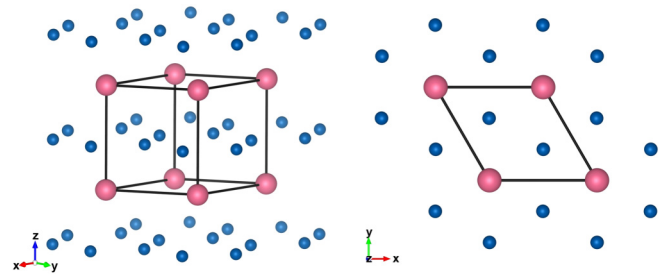

FIG. 1. Side and top view of MB_2 hexagonal crystal structure (space group $P6/mmm$). The structure has stacked up alternate layers of metal (pink) and boron (blue) atoms.

The atomic forces to determine IFCs for perfect and defect structures are calculations using density functional theory (DFT) package Quantum Espresso [39–44]. 5×5×4 supercells of ZrB_2 and HfB_2 are considered for IFC calculations. Second- and third-order IFCs are extracted as implemented in Phonopy and thirdorder.py respectively [33,45]. Further computational details and expressions for different perturbations **V** are found in the Supplemental Material (SM) [46].

III. RESULTS AND DISCUSSION

A. Atomic structure and phonons

Figure 1 shows the hexagonal crystal structure of MB_2 with alternate stacking of metal and boron layers (space group $P6/mmm$). Both the boron and metal layers are planar with covalent and metallic bonding nature, respectively. The interlayer bonding in MB_2 has mixed ionic and covalent behavior [15,47,48]. With such bonding, MB_2 has a compact unit cell with three atoms (one metal and two borons) and only slight differences in the $\perp$ and $\parallel$ lattice parameters ($c/a \gtrsim 1$). The obtained relaxed cell parameters for ZrB_2 are $a = 3.17$ Å, $c = 3.54$ Å, and HfB_2 are $a = 3.13$ Å, $c = 3.47$ Å, which are in good agreement with literature (see SM for details) [46,49,50].

Phonon dispersion curves for ZrB_2 and HfB_2 are shown in Fig. 2. Several overlapping features could be seen for these compounds due to their same crystal structures and the fact that Hf and Zr are iso-group elements. For both MB_2, there are in total nine phonon branches at a given q-point (three acoustic and six optic branches) and a similar dispersive nature of these branches is seen in the IBZ path. The differences in the phonon dispersion are mainly seen in the phonon frequency range and acoustic-optic gap. ZrB_2 with larger unit-cell volume ($\Omega = 31.059$ Å^3) has slightly narrower frequency range than HfB_2 ($\Omega = 29.87$ Å^3). Bonds are stiffer in HfB_2 than ZrB_2. Thus, HfB_2 bonds can be imagined as stronger springs with larger IFCs, leading to a wider phonon frequency range. Figure 2 also shows acoustic-optic energy gaps for both ZrB_2 and HfB_2, however with different widths. The acoustic-optic (a-o) gap is due to mass variations of the constituting elements (here, $\frac{m_{\text{Zr}}}{m_{\text{B}}} = 8.44$, $\frac{m_{\text{Hf}}}{m_{\text{B}}} = 16.51$), as heavier elements contribute majorly to the low-frequency modes and vice versa ($\omega \propto 1/\sqrt{m}$). Furthermore, as the transition metal mass increases, m_{Hf} (= 174.49 amu) > m_{Zr} ({=} 91.22 amu), the frequencies of acoustic modes are lowered

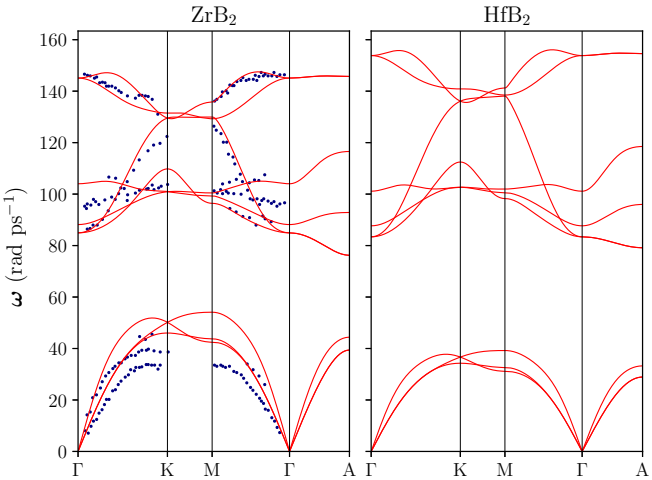

FIG. 2. Phonon dispersion of ZrB_2 and HfB_2. The calculations (lines) are compared with the available experiments (dots) for ZrB_2(0001) surface phonons [38].

in HfB_2. The calculated phonon dispersion of ZrB_2 is further compared with available experiments on surface phonons of ZrB_2(0001) produced by electron energy loss spectroscopy [38]. Surface termination leads to interlayer bond breaking, which affects the force constants and softens the acoustic modes than in bulk [38]. To our knowledge, no experiments on "bulk phonons" are found in literature. Overall, we find a good agreement with the experiments and previous *ab initio* investigations [15,51].

B. Thermal conductivity of MB_2

A fair intuition of κ_l of a material could be gained from its phonon dispersion. A large a-o phonon gap reduces anharmonic scattering and thus could lead to high thermal conductivity [30,32]. Similarly, higher phonon group velocities, obtained as $\partial\omega/\partial\mathbf{q}$, contribute to a higher κ_l. However, a further detailed comment requires explicit calculation of the phonon relaxation time τ and κ_l.

Firstly, we take up the pristine cases of ZrB_2 and HfB_2. Considering a large variation in the literature values [6,7,20,21,24,52], we perform a convergence analysis of κ_l at first. The experimental literature values considered here are only the lattice contribution of measured thermal conductivity given in Refs. [7,20,52]. These are obtained by separating out significant electronic contributions in such ceramics originating from their metallic behavior [52,53]. Figure 3 (inset) shows ZrB_2 and HfB_2 κ_l variation with respect to the cut-off radius ($r_{\text{cut-off}}$) used for the IFC calculations. Only within this $r_{\text{cut-off}}$, the double atomic displacements are considered while calculating third order IFCs for τ_{anh}^{-1}. The analysis is done at two different temperatures and we find convergence for a large $r_{\text{cut-off}}$ of ~6.5 Å (9th atomic neighbor shell). This analysis helps to avoid the ambiguity of a higher κ_l reported previously [24,25], that could result from using a randomly chosen small $r_{\text{cut-off}}$.

The κ_l variation with temperature is shown in Fig. 3, where ZrB_2 has lower κ_l than HfB_2 due to a stronger τ_{anh}^{-1} for ZrB_2, Fig. 4. This originates from both (a) smaller a-o gap and (b)

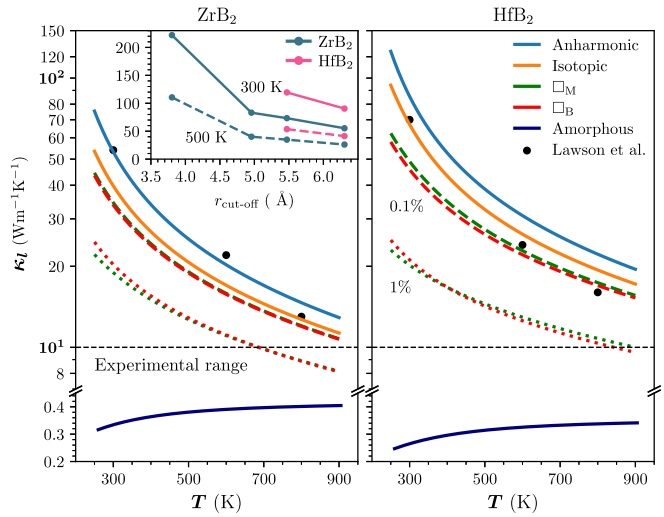

FIG. 3. κ_l variation with T for ZrB_2 and HfB_2 including different phonon scattering contributions. 0.1% and 1% defect concentrations are considered to elucidate the similar effect of $\square_M$ and $\square_B$ defects over a range of temperatures. Our results are compared with previous calculations by Lawson *et al.* [6] and a general experimental range of lattice part of thermal conductivity found in most of the literature [7,21] (excluding outliers [20]). Inset shows κ_l convergence for ZrB_2 and HfB_2 with respect to the IFC cut-off radius ($r_{\text{cut-off}}$).

larger cell volume of ZrB_2. At 300 K, κ_l for ZrB_2 is nearly half of that of HfB_2. We also include the effect of isotope scattering—a reportedly significant phonon scattering mechanism for wide a-o gap materials [54]. τ_{iso}^{-1} and τ_{anh}^{-1} variation with ω are shown in Fig. 4. The expected behavior of τ_{iso}^{-1} prominence at high ω is seen for MB_2, where τ_{iso}^{-1} is of the same order of magnitude as τ_{anh}^{-1}. A substantial effect of the isotope scattering on thermal conductivity is seen over a range of temperatures, with a reduction of 25% and 21% at 300 K for ZrB_2 and HfB_2, respectively, arising due to the mass variances

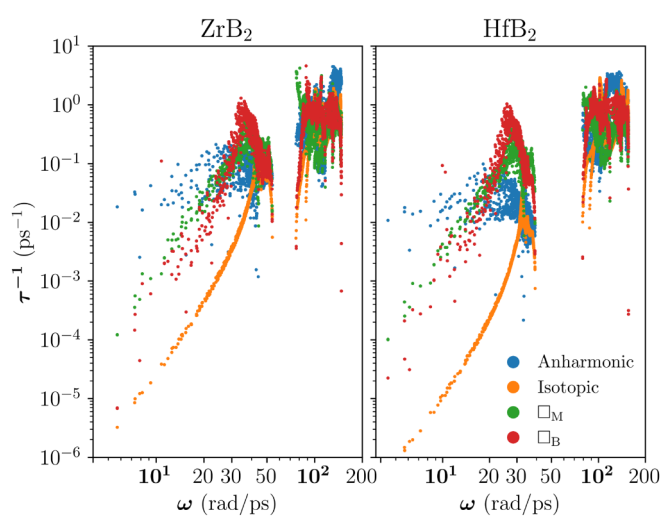

FIG. 4. Phonon scattering contributions from other phonons at 300 K, natural isotopes and vacancy defects in ZrB_2 and HfB_2 as a function of ω. Vacancy concentration of 1% is considered here for both $\square_M$ and $\square_B$.

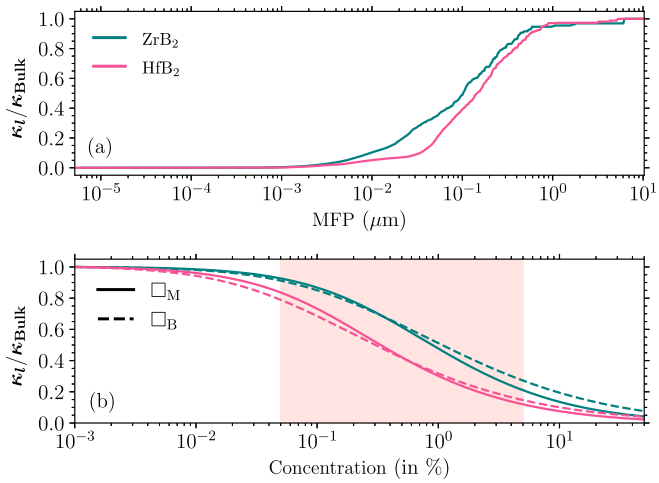

FIG. 5. Variation of κ_l/κ_{Bulk} at 300 K (a) with respect to phonon mean free path (MFP) contributions, and (b) as a function of defect concentration.

(g) of mostly the heavier elements in the compounds ($g_{Zr} = 3.42\times10^{-4}$, $g_{Hf} = 5.29\times10^{-5}$) [55]. The effect of isotope scattering can thus be reduced by synthesizing isotopically enriched samples. Excellent findings on isotopic enrichment have recently been reported for boron nitride [56].

C. Effective grain sizes

The differences in the experiments and our calculations of κ_l are still large, Fig. 3 (labelled "Isotopic"). Such a difference cannot be explained by only a strong phonon-electron scattering in MB_2. Yang *et al.* reported 38% reduction in κ_l of ZrB_2 considering phonon-electron interactions, although still higher than the experiments [25]. Moreover, this interaction is expected to be weaker in HfB_2 due to a wider a-o gap. This hints toward the presence of crystallographic defects in the samples, such as grain boundaries and native point defects, manifesting themselves as strong phonon scatterers. As most of the experiments have reported a low κ_l [7,20,21], such defects seem to appear naturally and more frequently during the synthesis of MB_2, specially when no other doping or phase mixing is reported.

Grains smaller than the mean free path (MFP) of the phonons will interfere with phonon propagation, whereas larger grain sizes would have no substantial phonon scattering effect. Previous experiments on ZrB_2 and HfB_2 have reported grain sizes of the order of a few microns in their samples [7,20]. To gauge their effectiveness in reducing the κ_l, we calculated the mode-wise cumulative contribution of κ_l at 300 K as a function of phonon MFP, Fig. 5(a). We find that ~85% of the κ_l contributions are from the phonons of MFP = 10 nm-1 μm for both ZrB_2 and HfB_2. Thus, grain sizes $>1\mu$m are unlikely to strongly scatter phonons to witness a very low κ_l seen in experiments.

D. Effect of vacancies

Native defects such as elemental vacancies, antisites, and interstitials could be inherent during material synthesis. Out of these, the antisite and interstitial defects in MB_2 are found to be energetically unfavorable [15,27]. In fact, our preliminary phonon calculations for B_{Zr} antisites show dynamical instability [46]. Metal and boron vacancies, even though having positive formation energies (see Ref. [46] for our calculations of defect energetics following Refs. [57,58]), are shown to be more stable than other defects along with their reported occurrences in MB_2 [26,27,58–62].

TABLE I. κ_l values at 300 K for ZrB_2 and HfB_2 from our calculations by gradually including anharmonic scattering, isotope scattering and defect scattering (1% concentration), and within amorphous limit. The results are compared with the experiments (only lattice contribution) [7,20]. Multiple values correspond to different samples in the study with the mentioned averaged grain sizes in bracket. Large variation in experiments is evident.

		κ_l ($Wm^{-1}K^{-1}$)	
		ZrB_2	HfB_2
	Anharmonic	53.20	85.46
	Isotopic	39.78	67.24
This paper	$\square_B$ (1%)	20.30	21.12
	$\square_M$ (1%)	18.94	20.19
	Amorphous	0.33	0.26
Expt.	Ref. [20]	23	
	Ref. [7]	6.25	9.09 (5.5 μm)
	”		0.6 (10.7 μm)

Defects change the local environment of charge distribution, mass density, chemical bonding, which are static properties but affect the forces seen by dynamic properties. Vacancy defects exhibit their effect through change in these properties only and hence are phenomenologically treated like any other point defect. However, vacancies could create relatively larger distortion in the lattice than other point defects due to the absence of atom and consequently broken local bonds. These distortions act as strong scattering centres for phonons [32,63]. The $\tau^{-1}_{\square_M}$ and $\tau^{-1}_{\square_B}$ are calculated using Eq. (2) for given vacancy concentrations, Fig. 4, to further compute κ_l. Figure 3 shows the variation of κ_l with temperature for only two concentrations—a low (0.1%) and a high (1%) concentration respectively, whereas κ_l as a function of vacancy concentration at $T = 300$ K is presented in Fig. 5. Noticeable effects of both $\square_M$ and $\square_B$ on κ_l are seen, Table I and Fig. 3. For ZrB_2, κ_l reduction (at 300 K) of 13% and 15% is seen for 0.1% of $\square_M$ and $\square_B$ respectively, which increases up to 52% and 49% for 1% defects. Similar trend is seen for HfB_2 with κ_l reduction of 27% and 32% for 0.1% and 70% and 69% for 1% of $\square_M$ and $\square_B$, respectively.

One of the striking features seen in our results is the similar effect of $\square_M$ and $\square_B$ on κ_l. The similarity is seen across a wide range of temperatures and concentrations, Figs. 3 and 5. For a quantitative understanding, we introduce a κ_l similarity measure (S_{κ_l}) by calculating the geometric mean of the ratio of $\kappa_{l,\square_M}$ and $\kappa_{l,\square_B}$ as

$$S_{\kappa_l} = \left(\prod_{i=0}^{n} \kappa_{l,\square_M}/\kappa_{l,\square_B}\right)^{1/n},$$

where index i runs through the temperature (T = 250 − 900 K) and concentration (c = 10^{-3} – 10%) individually to

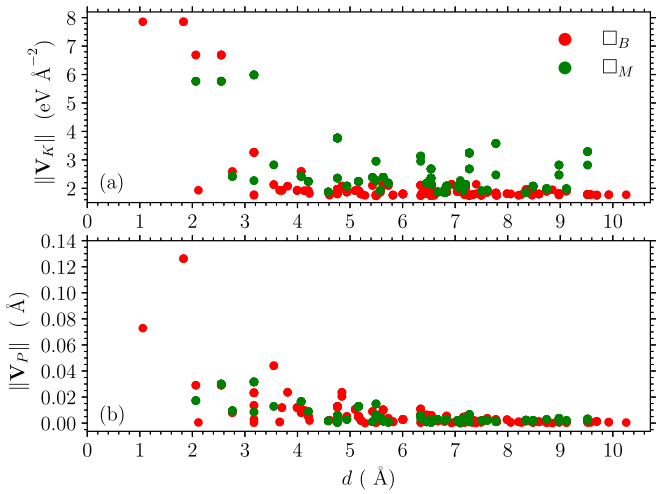

FIG. 6. Squared-L_2 norm of the perturbations (a) IFCs ($\mathbf{V}_K$) and (b) atomic positions ($\mathbf{V}_P$) with reference to the distance from the vacancy (d) for $\square_M$ and $\square_B$ vacancies respectively in ZrB_2. Strong, short ranged IFC perturbations are seen for $\square_B$, in contrast to weaker, long-ranged perturbations for $\square_M$. Similar trends are seen for HfB_2 in the SM [46].

give $S_{\kappa_l,T}$ and $S_{\kappa_l,c}$, respectively. S_{κ_l} should be $\sim$1 to exhibit a good similarity, which we clearly see in our results with $S^{0.1\%}_{\kappa_l,T}$, $S^{1\%}_{\kappa_l,T}$, $S^{300\,\mathrm{K}}_{\kappa_l,c}$ equal to 0.99, 1.02, 1.12 for ZrB_2 and 0.96, 0.99, 1.08 for HfB_2, respectively. Such a trend is due to comparable phonon scattering rates of $\square_M$ and $\square_B$, Fig. 4. The comparison is further explained by finding a Pearson's correlation coefficient of 0.97 in $\tau^{-1}_{\square_M}$ and $\tau^{-1}_{\square_B}$ using isotonic regression. This is surprising because boron is less than half the size of and around an order of magnitude lighter than Zr and Hf. Thus, a common understanding is that the transition metal vacancies scatter phonons more strongly than boron vacancies. This is also true in the case of Klemens model that considers vacancy perturbations as $\mathbf{V} = -m_\square - 2\langle\bar{m}\rangle$, where $m_\square$ is the mass of vacancy and $\langle\bar{m}\rangle$ the average atomic mass in the lattice [64–66]. Thus, Klemens model suggests a stronger phonon scattering by $\square_M$ due to a higher mass perturbation than $\square_B$. However, the explicit consideration of the IFC perturbations ($\mathbf{V}_K$) in our *ab initio* Green's function approach reveals a prominent effect of $\square_B$ irrespective of its smaller size.

To investigate deeper, we looked into the perturbations created by both the vacancies in MB_2, Fig. 6. The squared-L_2 norm of $\mathbf{V}_K$ is plotted as a function of the distance from the vacancy (d). $\|\mathbf{V}_K\|$ for $\square_B$ is stronger in the neighborhood of the vacancy site than that for $\square_M$, and the effect drops quickly with increase in d. In contrast, $\square_M$ exhibit a long-range effect in its perturbations. Perturbations in atomic positions ($\mathbf{V}_P$) are also found to be more for $\square_B$, suggesting that the prime cause of strong $\tau^{-1}_{\square_B}$ stems from large atomic displacements near the vacancy, Fig. 6(b). On the other hand, $\square_M$ shows some atomic rearrangements only near the defect site. This extraordinary behavior in ZrB_2 and HfB_2 comes from peculiar nature of their bonding. Study of electron localization function (ELF) by Lawson *et al.* [15] highlights the covalent bonding in B layers and metallic bonding between M layers. Covalent bonding is known to be stronger and directional in space, breaking of which leads to an increased local entropy and strong perturbations than for the case of metallic bonding. Consequently, we see $\tau^{-1}_{\square_M} \sim \tau^{-1}_{\square_B}$ in ZrB_2 and HfB_2, a phenomenon, which could be present in other diborides too. Boron is previously found to be a super scatterer in SiC too, exhibiting resonant phonon scattering [30].

Figure 5 further elucidates the region of maximum impact of $\square_M$ and $\square_B$ on κ_l at a given temperature. A sharp reduction in κ_l is seen for the vacancy concentrations $\sim$0.05%–5%, a range that has also been studied for stability and superconductivity in MB_2 [26,58–61]. κ_l flattens for concentrations $<$0.01% and $>$10%, where τ^{-1}_{anh} leads in the former case and $\tau^{-1}_{\square_{M/B}}$ in the latter.

E. Amorphous limit

Finally, to find the lower bound of κ_l in MB_2, we have calculated the amorphous limit of κ_l using Cahill's model that has previously shown good agreement with experiments [67,68]. This lower limit could give an estimation of κ_l at extremely high temperatures. As proposed by Cahill *et al.* [67] phonon lifetimes in the case of highly disordered structures are taken to be half of their oscillation periods, $\tau = \pi/\omega$. Using these phonon lifetimes and full phonon dispersion, we calculate the thermal conductivity of ZrB_2 and HfB_2. The obtained results are shown in Fig. 3, where $\kappa_l < 0.5$ Wm^{-1}K^{-1} is found for both MB_2. In contrast to the bulk case, HfB_2 has slightly lower κ_l in the amorphous case than ZrB_2, which is primarily because of higher phonon velocities in ZrB_2 (calculated speed of sound, $v_{s_{ZrB_2}} = 7.2$ Km s^{-1} $> v_{s_{HfB_2}} = 5.3$ Km s^{-1}). It is worth noting that amorphous κ_l are around two orders of magnitude smaller than the experiments for both MB_2, Table I, which indicates that the samples with more disorder and defects could show further low κ_l in experiments. This is an important aspect while designing for both low and high thermal conductivity applications of these high-temperature ceramics.

IV. CONCLUSIONS

To conclude, we have studied crucial effects of $\square_M$ and $\square_B$ on the κ_l of ZrB_2 and HfB_2. Our results reveal a large effect of smaller boron vacancy having a similar phonon scattering strength as that of bigger metal vacancy. We have explained this behavior due to strong local perturbation created by boron vacancies. We have also elaborated on other phonon scattering contributions such as isotopes and grain boundaries, where we majorly find that the effective grain sizes for these materials are in the range <1 μm. Furthermore, the amorphous limit of the lattice thermal conductivity is also explored, which serves as the lower bound limit of κ_l. We find that $\square_M$ and $\square_B$ play an important role in explaining the experimentally found low lattice thermal conductivity for these diborides. Along with different phonon scattering mechanisms studied in this paper, it is worth to mention about recently investigated significance of four-phonon scattering in materials with large a-o gaps like BAs [69]. Four-phonon scattering is although found to be less effective at room temperature for ultrahigh-temperature

ceramic ZrC [70], a detailed study in this respect for MB_2 in future would be certainly informative.

Overall our results serve the aim of predictive materials modeling by providing the guidelines to tune the thermal conductivity of ZrB_2 and HfB_2. A large control on κ_l could be achieved by managing the concentrations of $\square_M$ and $\square_B$ in the samples according to the application. In fact, we reveal a surprising prominence of $\square_B$ in MB_2 and a striking behavior of "*site independent phonon-vacancy scattering*", which could be explored in other materials too having a mixed bonding character. Furthermore, our results for pure crystals (only τ_{anh}^{-1}) also show that the intrinsic lattice contributions to the thermal conductivity in these ceramics is large, which could be further improved by isotope enrichment. Considering the experimental challenge in tuning the thermal conductivity lies in finding a middle way between the competing density and purity parameters of the samples. With this view, our study provides crucial material design aspects for range of applications for which these metal diborides are actively investigated.

ACKNOWLEDGMENTS

This work is supported by ISRO-RESPOND project (Project No. 190). A.K. also acknowledges the support from DST-INSPIRE Faculty Scheme (Grant No. IFA17-MS122) and NSM Brahma Super-computing Facility.

[1] C. Lu and C. Chen, Indentation strengths of zirconium diboride: Intrinsic versus extrinsic mechanisms, J. Phys. Chem. Lett. **12**, 2848 (2021).

[2] J. Gild, Y. Zhang, T. Harrington, S. Jiang, T. Hu, M. C. Quinn, W. M. Mellor, N. Zhou, K. Vecchio, and J. Luo, High-entropy metal diborides: A new class of high-entropy materials and a new type of ultrahigh temperature ceramics, Sci. Rep. **6**, 37946 (2016).

[3] V. Mohanavel, M. Ravichandran, V. Anandakrishnan, A. Pramanik, M. Meignanamoorthy, A. Karthick, and M. Muhibbullah, Mechanical properties of titanium diboride particles reinforced aluminum alloy matrix composites: A comprehensive review, Adv. Mater. Sci. Eng. **2021**, 7602160 (2021).

[4] P. Lazar, X.-Q. Chen, and R. Podloucky, First-principles modeling of hardness in transition-metal diborides, Phys. Rev. B **80**, 012103 (2009).

[5] E. Zapata-Solvas, D. Daniel, H. Lin, P. Brown, and W. Lee, Mechanical properties of ZrB_2 and HfB_2-based ultra-high temperature ceramics fabricated by spark plasma sintering, J. Eur. Ceram. Soc. **33**, 1373 (2013).

[6] J. Lawson, M. Daw, and C. Bauschlicher, Lattice thermal conductivity of ultra high temperature ceramics ZrB_2 and HfB_2 from atomistic simulations, J. Appl. Phys. **110**, 083507 (2011).

[7] L. Zhang, D. A. Pejaković, J. Marschall, and M. Gasch, Thermal and electrical transport properties of spark plasma-sintered HfB_2 and ZrB_2 ceramics, J. Am. Ceram. Soc. **94**, 2562 (2011).

[8] I. R. Shein and A. L. Ivanovskii, Influence of lattice vacancies on the structural, electronic, and cohesive properties of niobium and molybdenum borides from first-principles calculations, Phys. Rev. B **73**, 144108 (2006).

[9] M. Weiss, H. Riedl, V. Moares, P. H. Mayrhofer, and A. Limbeck, Laser based analysis of transition metal boride thin films using liquid standards, Microchem. J. **152**, 104449 (2020).

[10] A. Yousaf, M. Gilliam, L.-Y. Chang, M. Augustin, Y. Guo, F. Tahir, M. Wang, A. Schwindt, X. Chu, D. Li, S. Kale, A. Debnath, Y. Liu, M. Green, E. Santos, A. Green, and Q. Wang, Exfoliation of quasi-two-dimensional nanosheets of metal diborides, J. Phys. Chem. C **125**, 6787 (2021).

[11] J. Nagamatsu, N. Nakagawa, T. Muranaka, Y. Zenitani, and J. Akimitsu, Superconductivity at 39 K in magnesium diboride, Nature (London) **410**, 63 (2001).

[12] N. Barbero, T. Shiroka, B. Delley, T. Grant, H. Ott, and J. Mesot, Doping-induced superconductivity of ZrB_2 and HfB_2, Phys. Rev. B **95**, 094505 (2017).

[13] M. Bhatia, M. D. Sumption, E. W. Collings, and S. Dregia, Increases in the irreversibility field and the upper critical field of bulk MgB_2 by ZrB_2 addition, Appl. Phys. Lett. **87**, 042505 (2005).

[14] W. E. Lee, E. Giorgi, R. Harrison, A. Maître, and O. Rapaud, Nuclear applications for ultra-high temperature ceramics and max phases, in *Ultra-High Temperature Ceramics* (John Wiley & Sons, New York, 2014), Chap. 15, pp. 391–415.

[15] J. Lawson, C. Bauschlicher, and M. Daw, Ab initio computations of electronic, mechanical, and thermal properties of ZrB_2 and HfB_2, J. Am. Ceram. Soc. **94**, 3494 (2011).

[16] F. Monteverde, A. Bellosi, and L. Scatteia, Processing and properties of ultra-high temperature ceramics for space applications, Mater. Sci. Eng.: A **485**, 415 (2008).

[17] W. S. Williams, High-temperature thermal conductivity of transition metal carbides and nitrides, J. Am. Ceram. Soc. **49**, 156 (1966).

[18] R. Savino, L. Criscuolo, G. D. Di Martino, and S. Mungiguerra, Aero-thermo-chemical characterization of ultra-high-temperature ceramics for aerospace applications, J. Eur. Ceram. Soc. **38**, 2937 (2018).

[19] Y. Zhang, S. Liu, X. Zhou, G. Zhao, J. Liu, H. Shen, Z. Cai, X. Zhao, and L. Xiao, Ultra-high temperature oxidation behavior of ZrB2/YSZ modified Si-Mo-W coating with a diffusion barrier on niobium alloy, Corrosion Sci. **195**, 109977 (2022).

[20] J. W. Zimmermann, G. E. Hilmas, W. G. Fahrenholtz, R. B. Dinwiddie, W. D. Porter, and H. Wang, Thermophysical properties of ZrB_2 and ZrB_2-SiC ceramics, J. Am. Ceram. Soc. **91**, 1405 (2008).

[21] M. J. Thompson, W. G. Fahrenholtz, and G. E. Hilmas, Elevated temperature thermal properties of ZrB_2 with carbon additions, J. Am. Ceram. Soc. **95**, 1077 (2012).

[22] D. Mcclane, W. Fahrenholtz, and G. Hilmas, Thermal properties of $(Zr, TM)B_2$ solid solutions with $TM = Hf, Nb, W, Ti$, and y, J. Am. Ceram. Soc. **97**, 1552 (2014).

[23] D. Mcclane, W. Fahrenholtz, and G. Hilmas, Thermal properties of $(Zr, TM)B_2$ solid solutions with $TM = Ta, Mo, Re, V$, and Cr, J. Am. Ceram. Soc. **98**, 1552 (2014).

[24] H. Xiang, J. Wang, and Y. Zhou, Theoretical predictions on intrinsic lattice thermal conductivity of ZrB_2, J. Eur. Ceram. Soc. **39**, 2982 (2019).

[25] J. Y. Yang, W. Zhang, C. Xu, J. Liu, L. Liu, and M. Hu, Strong electron-phonon coupling induced anomalous phonon transport

in ultrahigh temperature ceramics ZrB2 and TiB2, Int. J. Heat Mass Transf. **152**, 119481 (2020).

[26] I. R. Shein, N. I. Medvedeva, and A. L. Ivanovskii, Effect of metal vacancies on the band structure of Nb, Zr, and Y diborides, Phys. Solid State **45**, 1617 (2003).

[27] E. Johansson, F. Eriksson, A. Ektarawong, J. Rosen, and B. Alling, Coupling of lattice dynamics and configurational disorder in metal deficient $Al_{1-\delta}B_2$ from first-principles, J. Appl. Phys. **130**, 015110 (2021).

[28] G.-J. Zhang, W.-M. Guo, D. W. Ni, and Y.-M. Kan, Ultrahigh temperature ceramics (UHTCs) based on ZrB_2 and HfB_2 systems: Powder synthesis, densification and mechanical properties, J. Phys.: Conf. Ser. **176**, 012041 (2009).

[29] J. Carrete, B. Vermeersch, A. Katre, A. V. Roekeghem, T. Wang, G. K. Madsen, and N. Mingo, Almabte: A solver of the space-time dependent boltzmann transport equation for phonons in structured materials, Comput. Phys. Commun. **220**, 351 (2017).

[30] A. Katre, J. Carrete, B. Dongre, G. K. H. Madsen, and N. Mingo, Exceptionally Strong Phonon Scattering by B Substitution in Cubic SiC, Phys. Rev. Lett. **119**, 075902 (2017).

[31] A. Katre, J. Carrete, and N. Mingo, Unraveling the dominant phonon scattering mechanism in the thermoelectric compound ZrNiSn, J. Mater. Chem. A **4**, 15940 (2016).

[32] A. Katre, J. Carrete, T. Wang, G. K. H. Madsen, and N. Mingo, Phonon transport unveils the prevalent point defects in GaN, Phys. Rev. Materials **2**, 050602(R) (2018).

[33] W. Li, J. Carrete, N. A. Katcho, and N. Mingo, ShengBTE: A solver of the Boltzmann transport equation for phonons, Comput. Phys. Commun. **185**, 1747 (2014).

[34] N. H. Protik, A. Katre, L. Lindsay, J. Carrete, N. Mingo, and D. Broido, Phonon thermal transport in 2H, 4H and 6H silicon carbide from first principles, Mater. Today Phys. **1**, 31 (2017).

[35] S. I. Tamura, Isotope scattering of dispersive phonons in Ge, Phys. Rev. B **27**, 858 (1983).

[36] S. I. Tamura, Isotope scattering of large-wave-vector phonons in GaAs and InSb: Deformation-dipole and overlap-shell models, Phys. Rev. B **30**, 849 (1984).

[37] N. Mingo, K. Esfarjani, D. A. Broido, and D. A. Stewart, Cluster scattering effects on phonon conduction in graphene, Phys. Rev. B **81**, 045408 (2010).

[38] T. Aizawa, W. Hayami, and S. Otani, Surface phonon dispersion of ZrB_2(0001) and NbB_2(0001), Phys. Rev. B **65**, 024303 (2001).

[39] P. Giannozzi, S. Baroni, N. Bonini, M. Calandra, R. Car, C. Cavazzoni, D. Ceresoli, G. L. Chiarotti, M. Cococcioni, I. Dabo *et al.*, Quantum espresso: A modular and open-source software project for quantum simulations of materials, J. Phys.: Condens. Matter **21**, 395502 (2009).

[40] P. Giannozzi, O. Andreussi, T. Brumme, O. Bunau, M. B. Nardelli, M. Calandra, R. Car, C. Cavazzoni, D. Ceresoli, M. Cococcioni *et al.*, Advanced capabilities for materials modelling with quantum espresso, J. Phys.: Condens. Matter **29**, 465901 (2017).

[41] P. Giannozzi, O. Baseggio, P. Bonfà, D. Brunato, R. Car, I. Carnimeo, C. Cavazzoni, S. de Gironcoli, P. Delugas, F. Ferrari Ruffino *et al.*, Quantum espresso toward the exascale, J. Chem. Phys. **152**, 154105 (2020).

[42] G. Kresse and D. Joubert, From ultrasoft pseudopotentials to the projector augmented-wave method, Phys. Rev. B **59**, 1758 (1999).

[43] P. E. Blöchl, Projector augmented-wave method, Phys. Rev. B **50**, 17953 (1994).

[44] J. P. Perdew, K. Burke, and M. Ernzerhof, Generalized Gradient Approximation Made Simple, Phys. Rev. Lett. **77**, 3865 (1996).

[45] A. Togo and I. Tanaka, First principles phonon calculations in materials science, Scr. Mater. **108**, 1 (2015).

[46] See Supplemental Material at http://link.aps.org/supplemental/10.1103/PhysRevMaterials.6.065403 for perturbations in IFCs and atomic positions with reference to the distance from vacancy for HfB_2, instability of B_{Zr} antisite, vacancy formation energies in MB_2, comparison of calculated lattice parameters with literature and further computational details.

[47] X. J. Wang, T. Mori, I. Kuzmych-Ianchuk, Y. Michiue, K. Yubuta, T. Shishido, Y. Grin, S. Okada, and D. G. Cahill, Thermal conductivity of layered borides: The effect of building defects on the thermal conductivity of $TmAlB_4$ and the anisotropic thermal conductivity of AlB_2, APL Mater. **2**, 046113 (2014).

[48] F. R. Wagner, A. I. Baranov, Y. Grin, and M. Kohout, A position-space view on chemical bonding in metal diborides with AlB_2 type of crystal structure, Z Anorg. Allg. Chem. **639**, 2025 (2013).

[49] H. Li, L. Zhang, Q. Zeng, J. Wang, L. Cheng, H. Ren, and K. Guan, Crystal structure and elastic properties of ZrB compared with ZrB_2: A first-principles study, Comput. Mater. Sci. **49**, 814 (2010).

[50] P. Vajeeston, P. Ravindran, C. Ravi, and R. Asokamani, Electronic structure, bonding, and ground-state properties of AlB_2-type transition-metal diborides, Phys. Rev. B **63**, 045115 (2001).

[51] H. Xiang, Z. Feng, Z. Li, and Y. Zhou, First-principles investigations on elevated temperature elastic and thermodynamic properties of ZrB_2 and HfB_2, J. Am. Ceram. Soc. **100**, 3662 (2017).

[52] G. J. K. Harrington and G. E. Hilmas, Thermal conductivity of ZrB_2 and HfB_2, in *Ultra-High Temperature Ceramics* (John Wiley & Sons, New York, 2014), Chap. 9, pp. 197–235.

[53] S. Li, A. Wang, Y. Hu, X. Gu, Z. Tong, and H. Bao, Anomalous thermal transport in metallic transition-metal nitrides originated from strong electron-phonon interactions, Mater. Today Phys. **15**, 100256 (2020).

[54] L. Lindsay, D. A. Broido, and T. L. Reinecke, Phonon-isotope scattering and thermal conductivity in materials with a large isotope effect: A first-principles study, Phys. Rev. B **88**, 144306 (2013).

[55] L. Lindsay, D. A. Broido, and T. L. Reinecke, First-Principles Determination of Ultrahigh Thermal Conductivity of Boron Arsenide: A Competitor for Diamond? Phys. Rev. Lett. **111**, 025901 (2013).

[56] K. Chen, B. Song, N. K. Ravichandran, Q. Zheng, X. Chen, H. Lee, H. Sun, S. Li, G. Gamage, F. Tian *et al.*, Ultrahigh thermal conductivity in isotope-enriched cubic boron nitride, Science **367**, 555 (2020).

[57] C. Bera, S. Jacob, I. Opahle, N. S. H. Gunda, R. Chmielowski, G. Dennler, and G. K. H. Madsen, Integrated computational materials discovery of silver doped tin sulfide as a thermoelectric material, Phys. Chem. Chem. Phys. **16**, 19894 (2014).

[58] M. Matas, A. Farhadizadeh, and J. Houska, Vacancies and substitutional defects in multicomponent diboride

$Ti_{0.25}Zr_{0.25}Hf_{0.25}Ta_{0.25}B_2$: First-principle study, J. Phys.: Condens. Matter **34**, 095901 (2022).

[59] S. Zhang and H. Sun, Effects of boron defects on mechanical strengths of TiB_2 at high temperature: *Ab initio* molecular dynamics studies, Phys. Chem. Chem. Phys. **22**, 6560 (2020).

[60] N. N. Greenwood, R. V. Parish, and P. Thornton, Metal borides, Q. Rev. Chem. Soc. **20**, 441 (1966).

[61] M. Dahlqvist, U. Jansson, and J. Rosen, Influence of boron vacancies on phase stability, bonding and structure of MB_2 (M = Ti, Zr, Hf, V, Nb, Ta, Cr, Mo, W) with AlB_2 type structure, J. Phys.: Condens. Matter **27**, 435702 (2015).

[62] W. Bao, S. Robertson, J. W. Zhao, J. X. Liu, H. Wu, G. J. Zhang, and F. Xu, Structural integrity and damage of ZrB_2 ceramics after 4 MeV Au ions irradiation, J. Mater. Sci. Technol. **72**, 223 (2021).

[63] N. A. Katcho, J. Carrete, W. Li, and N. Mingo, Effect of nitrogen and vacancy defects on the thermal conductivity of diamond: An *ab initio* Green's function approach, Phys. Rev. B **90**, 094117 (2014).

[64] P. G. Klemens, Thermal resistance due to point defects at high temperatures, Phys. Rev. **119**, 507 (1960).

[65] P. G. Klemens, The scattering of low-frequency lattice waves by static imperfections, Proc. Phys. Soc. A **68**, 1113 (1955).

[66] R. Gurunathan, R. Hanus, M. Dylla, A. Katre, and G. J. Snyder, Analytical models of phonon-point-defect scattering, Phys. Rev. Applied **13**, 034011 (2020).

[67] D. G. Cahill, S. K. Watson, and R. O. Pohl, Lower limit to the thermal conductivity of disordered crystals, Phys. Rev. B **46**, 6131 (1992).

[68] G. Coloyan, N. D. Cultrara, A. Katre, J. Carrete, M. Heine, E. Ou, J. Kim, S. Jiang, L. Lindsay, N. Mingo *et al.*, Basal-plane thermal conductivity of nanocrystalline and amorphized thin germanane, Appl. Phys. Lett. **109**, 131907 (2016).

[69] T. Feng, L. Lindsay, and X. Ruan, Four-phonon scattering significantly reduces intrinsic thermal conductivity of solids, Phys. Rev. B **96**, 161201(R) (2017).

[70] T. A. Mellan, A. Aziz, Y. Xia, R. Grau-Crespo, and A. I. Duff, Electron and phonon interactions and transport in the ultrahigh-temperature ceramic ZrC, Phys. Rev. B **99**, 094310 (2019).